Materials Science and Engineering A 534 (2012) 297–308

Contents lists available at SciVerse ScienceDirect

Materials Science and Engineering A

journal homepage: www.elsevier.com/locate/msea

Factors governing the mechanical behaviour of CrSiN coatings: Combined nanoindentation testing and transmission electron microscopy

P.C. Wo[a,*], P.R. Munroe[a], Z. Li[b], Z.-T. Jiang[c], Z.H. Xie[d], Z.F. Zhou[d,e], K.Y. Li[e]

[a] Electron Microscope Unit, University of New South Wales, Sydney, NSW 2052, Australia
[b] Southeast University, School of Materials Science and Engineering, Nanjing, PR China
[c] School of Engineering and Energy, Murdoch University, WA 6150, Australia
[d] School of Engineering, Edith Cowan University, Joondalup, WA 6027, Australia
[e] Department of Mechanical and Biomedical Engineering, City University of Hong Kong, Kowloon, Hong Kong, China

ARTICLE INFO

Article history:
Received 7 September 2011
Accepted 11 November 2011
Available online 1 December 2011

Keywords:
Transmission electron microscopy (TEM)
Nanoindentation
X-ray photoelectron spectroscopy (XPS)
Deformation structure
Coatings
Chromium silicon nitride

ABSTRACT

A direct link between the microstructure and mechanical properties of CrSiN coatings with varying Si contents was established by examining their microstructural evolution and deformation behaviour, enabled by cross-sectional transmission electron microscopy. A transformation from a columnar-grained structure, in the binary compound, to a nanocomposite structure, consisting of CrN nanocrystallites embedded in an amorphous matrix, was observed in the coating having a Si content of 28.5 at.%. The columnar-structured coatings were observed to deform by grain boundary shear sliding, whilst cracks occurred in nanocomposite coatings. Moreover, the coating having a Si content of 14.3 at.% exhibited the highest hardness as a result of grain boundary strengthening facilitated by Si_3N_4 segregation, together with solid solution strengthening of Si in CrN, the Hall–Petch effect for the finer CrN grains and a high compressive residual stress. A further increase of Si content to 28.5 at.% led to a reduction in hardness due to the high volume fraction of the amorphous phase, together with the presence of cracks in the as-deposited coating. The findings provide deeper insight into the origin of the mechanical behaviour of CrSiN coatings.

1. Introduction

Increasing demands on the performance of protective coatings under harsh conditions such as dry, high speed machining operation call for high hardness and good oxidation resistance. Chromium nitrides (CrN) have attracted considerable attention owing to their good combination of mechanical and thermal properties [1,2] compared to other nitrides of transition metals, such as TiN [3]. More recently, superhardness (hardness >40 GPa) has been achieved in titanium nitrides by the addition of Si that changes the microstructure from closely packed columnar TiN grains into TiN nanocrystals embedded in a Si_3N_4 amorphous matrix [4,5]. Such extremely high hardness is attributed to the combined effects of the fine grain size together with the strong interfacial bonding between the TiN nanocrystals and the surrounding amorphous phase. The same strategy has been applied to harden CrN coatings. Despite a similar microstructural evolution through Si additions to CrN, the hardness of CrSiN coatings obtained ranged from 24 to 32 GPa [2,6–9] and the improvements in hardness are less remarkable than those observed in the TiSiN system.

For CrSiN coatings with low Si contents (5.4 at.% [6], ~3 at.% [10] and ~0.7 at.% [7]), the increase in hardness was attributed to a solid solution of Si in crystalline CrN. At higher Si concentrations (up to ~13 at.%), the increase in hardness is usually attributed to the size reduction of CrN grains that frequently exhibit a {2 0 0} preferred orientation [2,6,7,11,12]. CrSiN coatings, exhibiting CrN grains with a {2 0 0} orientation were shown to be more resistant to deformation compared to coatings where the grains exhibited a {1 1 1} preferred orientation [10]. However, the hardness of coatings which exhibit strong textures may also be lowered by the presence of localised defects that involve 'tubes' of a lower density material, compared to surrounding phases [10,13]. This is because such defects tend to be aligned parallel to the film growth direction and so coatings that exhibit such localised defects may show less resistance to deformation when it is under a load normal to the coating surface.

Although a number of studies have examined the influence of Si on the microstructure and mechanical properties of CrN films, the factors that control the mechanical properties of the CrSiN coatings are poorly understood, primarily due to an absence of studies where the microstructure following deformation has been characterised.

* Corresponding author. Tel.: +61 2 9385 4425; fax: +61 2 9385 6400.
E-mail address: a.wo@unsw.edu.au (P.C. Wo).

0921-5093/$ – see front matter © 2011 Elsevier B.V. All rights reserved.
doi:10.1016/j.msea.2011.11.072

Recent detailed studies on deformation in TiSiN coatings [14,15], have provided an understanding of the role of microstructure in controlling the mechanical behaviour of these coatings.

In addition, it is well-known that coatings usually contain high compressive residual stresses [16–19]. Residual stress in CrN coatings has shown to have pronounced influence on both hardness [20] and fatigue strength [19]. However, the influence of Si content in CrSiN coatings on the magnitude of the residual stress and the consequent impact of this stress on mechanical behaviour is not known.

In this work, the microstructural changes of CrSiN coatings through the addition of Si were characterised using cross-sectional transmission electron microscopy (XTEM). The surface chemical composition of the coatings was studied by X-ray photoelectron spectroscopy (XPS). Then, the hardness, elastic modulus and residual stress of these coatings were determined by nanoindentation. Finally, the role of microstructure in controlling the mechanical properties of CrSiN coatings was clarified by examination of nanoindentation-induced subsurface deformation using XTEM.

2. Experimental

2.1. Deposition of coatings

The CrN and CrSiN coatings were deposited on AISI M2 tool steel substrates (heat treated to a hardness of HRC of 62) using a Teer UDP 650/4 closed field unbalanced magnetron sputtering system with a four-target configuration (Teer Coatings Ltd., Droitwich, Worcestershire, UK). The steel substrates were polished to an average surface roughness of ~0.03 μm before being loaded into the vacuum chamber. Prior to film deposition, the polished steel substrates were sputter cleaned with an Ar plasma at a bias voltage of −500 V for 30 min to remove oxide layers and other contaminants on the substrate surface. High purity Ar gas was pumped into the chamber at a rate of 50 sccm via a mass flow controller (MFC) (MKS Instruments, Inc., Andover, MA, USA) and the gas pressure was maintained at ~0.17 Pa during sputter cleaning. Before deposition of either CrN or CrSiN, a wetting layer of Cr (~0.2 μm) was deposited by supplying a DC current of 5.0 A to the two Cr targets for 3 min. This Cr layer serves to improve the adhesion between the nitride coating and the substrate. Throughout the film deposition process, the substrates were maintained at ~550 °C and rotated at a constant speed of 10 rpm. Two Cr and one Si targets, each having dimensions of about 380 mm × 175 mm × 10 mm, were used and the bias voltage was maintained at −80 V. Nitrogen reactive gas was introduced into the chamber for the formation of nitrides. The flow rate of N_2 gas was maintained by another MFC at a rate of 60 sccm. Four samples, namely one CrN binary coating and three CrSiN ternary coatings of different Si contents, were prepared. The three CrSiN coatings have increasing Si contents and hereafter are identified as CrSiN-1, CrSiN-2 and CrSiN-3 (Table 1). Various combinations of currents were supplied to the targets to produce samples with different Si contents, as summarised in Table 1. The silicon content in the four coatings was found to increase as either I_{Si} increased or I_{Cr} reduced (Table 1). The Si content of the samples was calculated from an expression Si/(Cr + Si + N) using results obtained from XPS (discussed below). Values listed in Table 1 are for reference only as oxygen was also detected from the near surface region of the coatings and may not represent the average Si content across the thickness of the coatings.

2.2. X-ray photoelectron spectroscopy

The composition and chemical bonding state for all four coatings were investigated by XPS. Before analysis, the samples were ultrasonically cleaned in acetone, alcohol and then distilled water, respectively, at room temperature. XPS analysis was then performed on the as-deposited samples with a Kratos-Axis Ultra spectrometer, using Mg Kα X-ray radiation ($h\nu$ = 1253.6 eV) with a background pressure of 10^{-9} Torr. The voltage and emission current of the X-ray source were maintained at 12 kV and 12 mA, respectively. Samples were mounted with copper tape with the coating surface normal to the entrance of the hybrid-mode electrostatic lens through a slot (iris = 0.6 and aperture = 49). A charge neutraliser was used during data acquisition. Data was calibrated against the copper Cu 2p peak, at 932.67 eV, the silver Ag 3d peak, at 368.27 eV, the 1s carbon peak (hydrocarbon) at 284.5 eV and the Au 4f peak at 83.98 eV. In each sample, a survey scan spectrum was first acquired with pass energy of 80 eV and 1 eV step size. High resolution core level XPS spectra for peaks associated with elements Cr, O, N, and Si were then obtained from each sample using pass energy of 10 eV and a finer step size of 0.1 eV for detailed analysis on the bonding states of these four elements. Background of the spectra were subtracted using the Shirley base-line method [21].

2.3. Nanoindentation and microstructural analyses

A nanoindentation workstation (Ultra-Micro Indentation System 2000, CSIRO, Sydney, Australia), equipped with a Berkovich indenter, was used to measure the hardness and elastic modulus of the coatings according to the Oliver–Pharr method [22]. Twenty indentations were performed on each of the four samples at indentation depths smaller than 10% of the coating thickness in order to avoid any influence from the substrate. For each test, 20 incremental and 20 decremental steps were taken under load control. Prior to the nanoindentation tests, the area function of the Berkovich indenter tip was calibrated using a standard fused silica specimen.

Nanoindentation was also carried out using a spherical indenter, having a radius of 5 μm, at a maximum load of 500 mN to introduce contact damage into the coatings. XTEM samples was then prepared using a focused ion beam (FIB) microscope (FEI XP 200, FEI, USA) through the middle of the indentations to facilitate examination of subsurface deformation. Samples were also made from undeformed locations for comparison.

Microstructural analysis of coatings' cross-sections was performed using a Philips CM 200 field emission gun TEM operating at 200 kV. The TEM was equipped with an energy dispersive X-ray spectroscopy (EDS) system for elemental analysis.

Indentation tests were also performed using the 5 μm radius spherical indenter at loads between 15 and 30 mN to study the residual stress in the as-deposited coatings using the methods developed by Swadener et al. [16].

3. Results

3.1. Microstructure of the CrSiN coatings

Cross-sections obtained from undeformed regions in the four coatings were used to characterise their as-deposited microstructure (Fig. 1(a)–(d)). In the binary CrN film, well-defined, closely packed columnar grains with their longer axis parallel to the film growth direction were observed. Similar gain structures can also be seen in the Cr wetting layer (Fig. 1(a)). Such a closely packed columnar microstructure can still be observed in both CrSiN-1 and CrSiN-2 (Fig. 1(b) and (c)), but the grains were finer and shorter than those with higher Si contents. A dramatic change in the microstructure occurred when the Si content was further increased to ~28.5 at.% (CrSiN-3), in which much finer and more equiaxed grains were found to be distributed uniformly within the matrix (Fig. 1(d)).

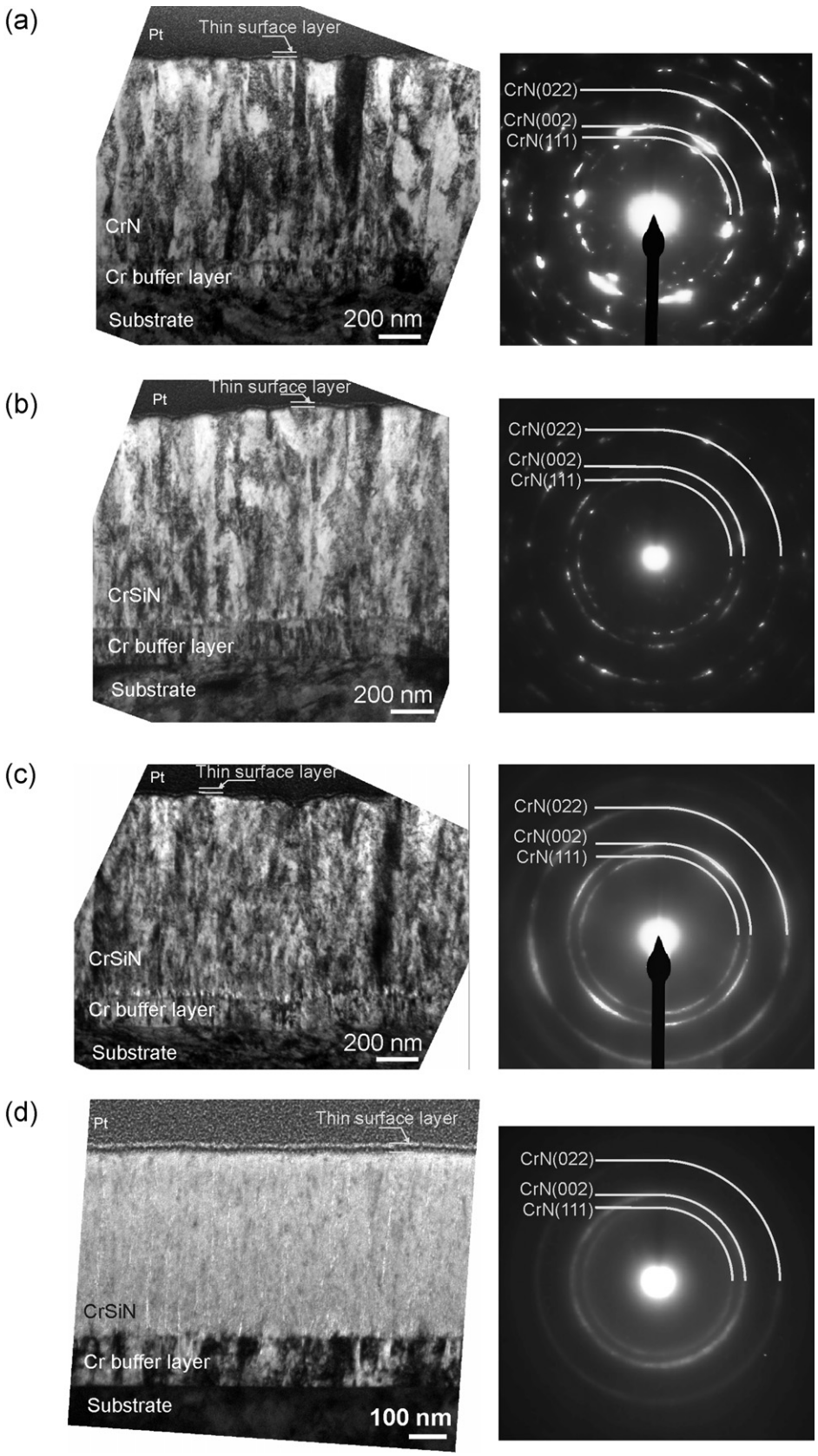

Fig. 1. Cross-sectional bright field TEM images and the corresponding SAD patterns of (a) the binary CrN coating, (b) CrSiN-1, (c) CrSiN-2 and (d) CrSiN-3. Diffraction rings for {1 1 1}, {0 0 2} and {0 2 2} are indexed in the SAD patterns.

Table 1
Target current and duration for the deposition of the CrN and CrSiN coatings in the four samples. The Si concentration is obtained from XPS measurements.

Sample ID	Si/(Cr + Si + N) (at.%)	Current to both Cr targets, I_{Cr} (A)	Current to the Si target, I_{Si} (A)	Deposition time (min)
Binary CrN	0.0	5	0	60
CrSiN-1	8.3	5	1	60
CrSiN-2	14.3	5	5	40
CrSiN-3	28.5	2	5	65

Table 2
Thickness of the CrSiN and Cr wetting layer in coatings measured from XTEM images obtained non-deformed areas.

	Total thickness (μm)	Thickness of CrSiN layer only (μm)	Thickness of Cr layer only (total-CrSiN layer) (μm)
Binary CrN (0 at.% Si)	1.004 ± 0.052	0.848 ± 0.042	0.155
CrSiN-1 (8.3 at.% Si)	1.170 ± 0.013	0.984 ± 0.010	0.186
CrSiN-2 (14.5 at.% Si)	1.061 ± 0.022	0.917 ± 0.020	0.144
CrSiN-3 (28.3 at.% Si)	0.641 ± 0.019	0.495 ± 0.013	0.146

Corresponding selected area diffraction (SAD) patterns of the four coatings are also shown in Fig. 1(a)–(d). Data from the Cr wetting layer and the protective Pt layer, which was deposited during XTEM preparation, were excluded when obtaining the SAD patterns. Discrete diffraction reflections can be seen in the SAD patterns of the CrN coating (Fig. 1(a)) and CrSiN-1 (Fig. 1(b)). Near-continuous segments of diffraction rings can be seen in the SAD pattern obtained from CrSiN-2 (Fig. 1(c)). In CrSiN-3, the diffraction rings are uniform and continuous (Fig. 1(d)). These continuous rings comprise a large number of reflections, suggesting that this coating is polycrystalline with a very fine grain size. The uniformity of the rings suggests that these grains are randomly oriented without any strong preference in orientation. In contrast, diffraction patterns showing discontinue diffraction 'rings' or spots suggest larger grains in some specific orientations. However, no obvious texture is apparent in the coatings with the lower silicon contents. The transition in the SAD patterns obtained from these four samples is consistent with the observations from the bright field TEM images that size of the grains in the CrSiN coatings reduces as the Si content increases.

Analysis of the diffraction patterns revealed that the rings obtained from all four samples corresponded to the Bragg reflections for fcc-structured CrN. Lattice parameters measured from the first three diffraction rings (indexed in the SAD patterns in Fig. 1) obtained in the binary CrN, CrSiN-1, CrSiN-2 and CrSiN-3 are 4.22 (±0.21), 3.98 (±0.07), 4.29 (±0.11) and 4.05 (±0.14) Å, respectively. The values in the brackets are the error estimated from the variations of the mean values calculated from $d_{(111)}$, $d_{(002)}$ and $d_{(022)}$ due to the uncertainty in measuring the diameters of the diffraction rings. The reported value for the lattice parameter of fcc CrN is 4.14 Å (JCPDS 11-0065) that lies within the range of the lattice parameters measured from all the samples. Notably, the lattice parameter of CrSiN-1 is slightly lower than the value for the binary compound. As the Si content increased to ~14.3 at.% (CrSiN-2), the measured lattice parameter is slightly higher than the value for the binary compound. A reduction of lattice parameter was also observed in other CrSiN coatings having low to medium Si concentration that were deposited by a hybrid arc ion plating and magnetron sputtering process, presumably caused by replacement of smaller Si atoms into Cr sites[12]. When the Si content was further increased, the Si may corporate into the lattice interstitial positions which causes expansion of the lattice and so a larger lattice parameter was observed in CrSiN-2 [10,23]. Both substitutional and interstitial of non-stoichiometric Si atoms in the CrN lattice suggests solid solution of Si in CrN. It is possible that the change in the microstructure may lead to a reduction of solubility limit of Si in CrN, and so the lattice parameter is restored to a value closer to the reported value for the binary compound [12].

Thickness measurements, from TEM micrographs of the four coatings, are shown in Table 2. The mean values of each sample were obtained from averaging >10 measurements. It can be seen that the binary CrN, CrSiN-1 and CrSiN-2 coatings have a similar thickness of ~1 μm, but CrSiN-3 is only ~0.6 μm thick. Clearly, the thickness of the CrSiN layer in CrSiN-3 is significantly less than that in the other samples. This is presumably because of the slower deposition rate due to the lower Cr target current used to deposit CrSiN-3 (see Table 1). In addition, for coating deposition in a constant nitrogen flow rate environment, as is the case in this study, a smaller Cr target current is more vulnerable to the so-called target "poisoning effect" [24], which refers to the formation of a compound film on the target surface that leads to a significant reduction in the deposition rate [25].

A high density of elongated fine cracks that are aligned parallel to the film growth direction can be observed in CrSiN-3 (Fig. 1(d)). Such cracks are not observed in the other coatings. Wang et al. [12] observed similar cracks in cross-sections of CrSiN coatings having Si contents between ~15 and 22 at.%. However, these authors did not discuss this particular feature in their coatings.

A thin layer between 12 and 15 nm in width can be identified at the outmost surface of all four coatings (indicated in Fig. 1(a)–(d)). This layer may be an artefact due to interaction of the specimens with either Pt or Ga ions during the XTEM sample preparation in the FIB. It may also be an oxide layer that formed on the coating surface as it was exposed to air after deposition [26,27]. Unambiguous analysis of this layer could not be achieved using TEM. Thus, XPS was carried out on the as-deposited coatings to investigate the nature of this layer.

3.2. Composition and bonding structure of the near surface region of the coatings

Cr, N and O on the coating surfaces were identified from the survey scan XPS spectra obtained from all four samples. For the three CrSiN coatings a Si peak was also observed. The concentration of each of these elements was obtained from the spectra, treated by Shirley background subtraction, using the Vision Processing software of the Kratos instrument and the results are listed in Table 3.

Table 3
Chemical composition at the near surface region of the as-deposited CrSiN coatings derived from XPS analysis.

Samples	Cr (at.%)	Si (at.%)	N (at.%)	O (at.%)
Binary CrN	33.2	0	34.9	31.9
CrSiN-1	22.2	5.0	33	39.3
CrSiN-2	18.3	8.3	31.6	41.2
CrSiN-3	15.1	18.5	31.2	35.2

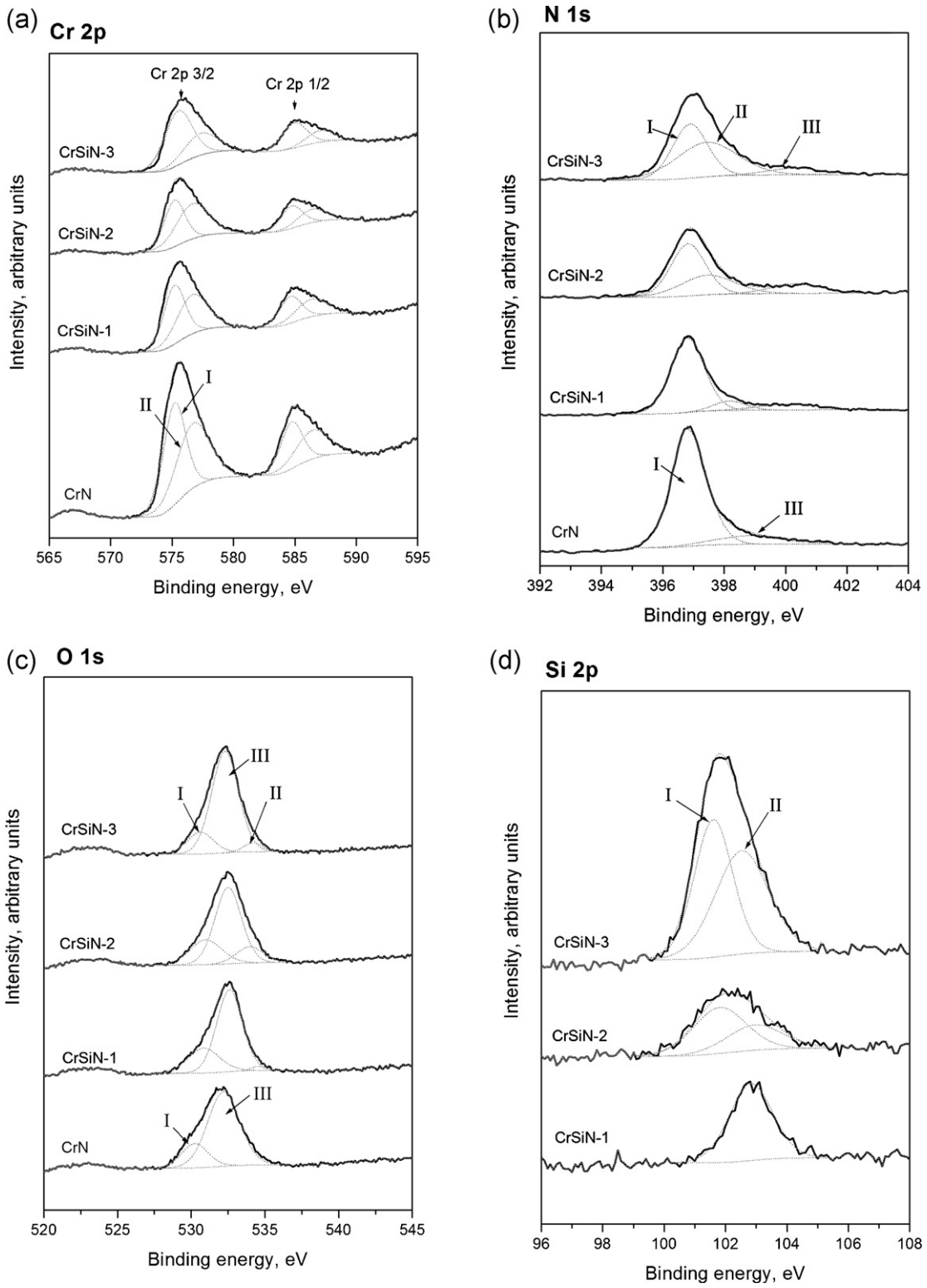

Fig. 2. High resolution (a) Cr 2p, (b) N 1s, (c) O 1s and (d) Si 2p XPS spectra for the four samples. The black solid lines are the experimental results. Deconvolution of the peaks is shown as grey dotted lines. Results of quantitative analysis of the deconvolution are shown in Table 4.

The curve-fitted high resolution XPS spectra of these four elements for all four coatings are shown in Fig. 2. The Cr 2p spectra of all the coatings (Fig. 2(a)) consisted of two peaks specifically for Cr 2p 3/2 and Cr 2p 1/2. The deconvoluted Cr 2p 3/2 peak was composed of two phases, namely CrN (575.2 eV) and Cr_2O_3 (576.7 eV). This indicates that some Cr was bonded to oxygen in the surface region across all the samples.

The N 1s spectrum for CrN (0 at.% Si) consisted of a principal peak from CrN (396.8 eV) and a weaker peak from Cr—O—N bonding (398.9 eV) (Fig. 2(b)). The presence of Cr—O—N bond might be ascribed to surface oxidation [28]. In addition to these two peaks, a component centred at 397.4 eV, which is most probably due to Si_3N_4 [29,30], was also deconvoluted in the N 1s spectra of all the CrSiN coatings (Fig. 2(b)). Since no well-defined diffraction ring

Table 4
Concentration of components observed from XPS results in the four CrSiN coatings.

Elements	Peaks indicated in Fig. 2	Possible bonding state	Percentage of the corresponding possible bonding state in each sample			
			Binary CrN (0 at.% Si)	CrSiN-1 (8.3 at.% Si)	CrSiN-2 (14.3 at.% Si)	CrSiN-3 (28.5 at.% Si)
N 1s	I	CrN	87.1	79.3	53.6	48.5
	II	Si_3N_4	–	11.1	31.7	43.2
	III	Cr—O—N	12.9	9.6	14.7	8.3
Cr 2p 3/2	I	CrN	51.0	50.8	60.4	67.3
	II	Cr_2O_3	49.0	49.2	39.6	32.7
Si 2p	I	SiO_x	–	–	32.6	49.1
	II	Si_3N_4	–	100.0	67.4	50.9
O1s	I	Cr_2O_3	27.7	31.4	16.1	17.3
	II	SiO_x	–	9.5	10.0	4.6
	III	H_2O, —OH	72.3	59.15	78.9	78.1

corresponding to Si_3N_4 was found in the SAD patterns (Fig. 1(b)–(d)), the Si_3N_4 phase in these three coatings is presumably amorphous in nature.

XPS spectra near the O 1s region obtained from the four samples are shown in Fig. 2(c). Only one peak appeared in this region. For the binary CrN coating, this peak was deconvoluted to a combination of Cr_2O_3 (530.9 eV) and OH^- (532.4 eV) phases. For all the other coatings, the O 1s peak shifted to a slightly higher binding energy level and an additional component at 534.4 eV, referring to the presence of SiO_x, was identified.

Analysis of the Si 2p spectra indicated that only Si—N bonds were present in CrSiN-1 (Fig. 2(d)). At higher Si contents (CrSiN-2 and CrSiN-3), this peak became broader and shifted to a lower binding energy level and can be fitted to a combination of SiO_x (101.6 eV) and Si_3N_4 (102.4 eV) phases (Fig. 2(d)).

Quantification of the components derived from deconvolution of the N 1s, Cr 2p, Si 2p and O 1s peaks observed from high-resolution XPS spectra of the four samples (Fig. 2) discussed above was carried out using the Casa XPS (V.2.3.15) software. The atomic concentration of all the components observed is listed in Table 4. According to the results obtained from the N 1s peak, the content of Si_3N_4 increased with Si content. In CrSiN-3, all the nitrogen was almost equally shared between bonding to Cr, forming CrN, and bonding to Si, forming Si_3N_4. This is in agreement with the TEM observations (Fig. 1(d)) in which a large number of CrN crystallites were embedded in the matrix, presumably Si_3N_4 in the case of CrSiN-3. In the CrSiN samples having lower Si contents, although most of the nitrogen is bonded to Cr, a considerable percentage of N in CrSiN-1 (11.1%) and in CrSiN-2 (31.7%) formed Si_3N_4. However, a second phase, besides CrN, is not observable in the TEM micrographs obtained from these two samples (Fig. 1(b) and (c)).

It was also observed in the binary CrN and CrSiN-1 coatings that Cr is almost equally bonded to O and N, whereas at higher Si contents, most of the Cr contributed to the formation of CrN. Table 4 also shows that most of the oxygen is identified as —OH bond, which is likely due to moisture in the ambient environment. Oxides in the form of Cr_2O_3 and SiO_x were also observed to be present.

3.3. Mechanical characterisation

Nanoindentation hardness, H, and elastic modulus, E, of the four coatings measured as a function of indentation contact depth are shown in Fig. 3(a) and (b), respectively. The H and E values were obtained from a narrow range of indentation depths between 0.08 and 0.11 μm, so that nanoindentation depth was <10% of the thickness of the coatings, where influence from the substrate is negligible. In contrast, by avoiding indentation at depths less than 0.08 μm the measurements are less likely to be subjected to the influences of instrumental error, surface roughness of the coating, surface contamination and the observed surface oxide film [31]. It was found that CrSiN-2 exhibited the highest H value of 35.8 ± 3.2 GPa.

From Fig. 3(b), it is observed that E of the binary CrN coating and CrSiN-1 are very similar, i.e. $E = 364 \pm 21$ GPa for binary CrN and $E = 368 \pm 21$ GPa for CrSiN-1. CrSiN-2 exhibits the highest E ($E = 397 \pm 21$ GPa), whereas the coating having the highest Si content (CrSiN-3) exhibited the lowest modulus ($E = 347 \pm 31$ GPa).

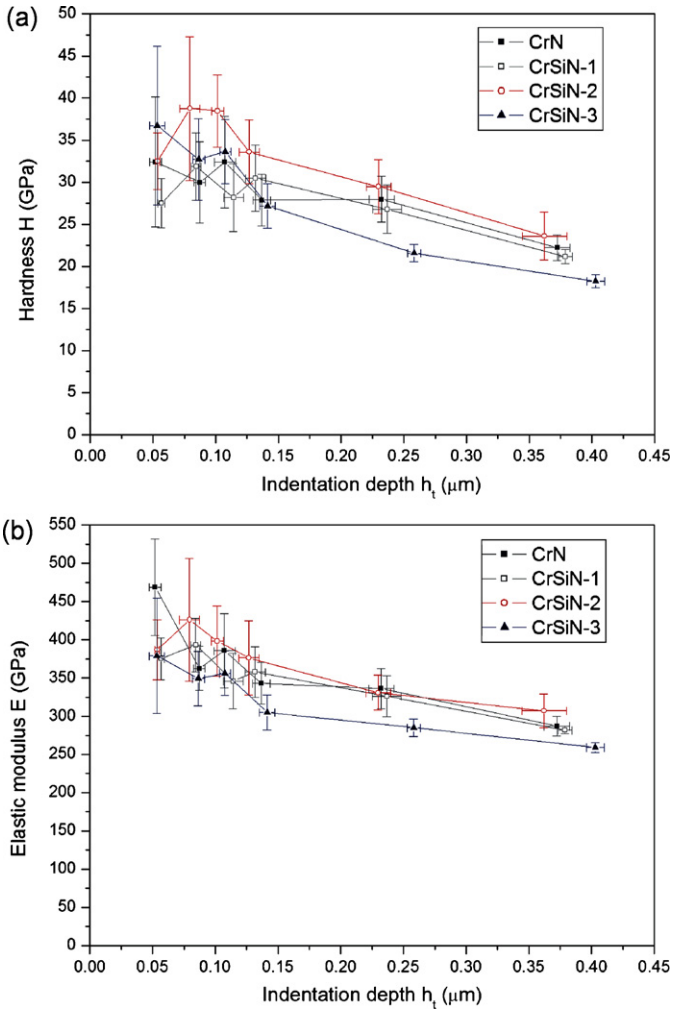

Fig. 3. Results obtained from nanoindentation tests for the four samples: (a) hardness and (b) elastic modulus as a function of indentation contact depth.

3.4. Residual stress in the coatings

The residual stress in the coatings was measured by nanoindentation. During indentation using a spherical indenter with a radius R, the mean contact pressure, P_m, in the elastically deforming material is given by:

$$P_m = \frac{4E^* a}{3\pi R} \quad (1)$$

where a is the contact radius. The effective elastic modulus, E^*, represents the elastic properties measured from the nanoindentation tests that involves the elastic properties of both the testing material and the indenter and is expressed as

$$E^* = \left(\frac{1-\nu_{indenter}^2}{E_{indenter}} + \frac{1-\nu_{sample}^2}{E_{sample}} \right)^{-1},$$

where ν is the Poisson ratio and E is the elastic modulus.

Taljai and Pharr [32] showed that when yielding occurs below the indenter along the indentation axis, P_m in the testing material is related to its biaxial residual stress σ^R and yield stress σ_y as:

$$P_m = 1.07(\sigma_y - \sigma^R) \quad (2)$$

Combining Eqs. (1) and (2) and rearranging, σ^R can be written as [16]:

$$\frac{\sigma^R}{\sigma_y} = 1 - \frac{1.25}{\pi}\left(\frac{E^* a_0}{\sigma_y R}\right), \quad (3)$$

where a_0 is the contact radius at the onset of yielding.

Swandener et al. [16] observed that the influence of residual stress on indentation measurement may be represented by plotting a graph of h_f/h_{max} against $E^*a/R\sigma_y$. The term $E^*a/R\sigma_y$ is a constant for a single material using a particular spherical indenter. The parameter h_f is the final indentation depth after load removal and h_{max} is the maximum indentation depth. The ratio h_f/h_{max} represents the relative amount of elastic and plastic deformation in the material. At the onset of plastic deformation, $h_f/h_{max} = 0$ and so the X-intercept of the curve would give the value of a_0 that is required to calculate σ^R using Eq. (3). To obtain this data, indentation tests were carried out at each of the four loads of 15, 20, 25 and 30 mN on all four coatings; more than 15 tests were carried out at each load. The values of a_0 for the samples were then obtained from extrapolating the experimental data to $h_f/h_{max} = 0$ as shown in Fig. 4(a).

The value of σ_y, roughly equals $H/3$ [33], which can be obtained from another set of nanoindentation data shown in Fig. 3(a). Similarly, value of E^* for the samples were obtained from Fig. 3(b).

Using the above results in Eq. (3), the residual stresses in all four samples was calculated and are shown in Fig. 4(b) with negative values representing compressive stress. In the binary CrN coating, $\sigma^R = -2.5$ GPa. The compressive stress increased with increasing Si content and reached a maximum value of −3.6 GPa in CrSiN-2. The compressive stress in the coating having the highest Si content (CrSiN-3) was reduced to −2.5 GPa.

3.5. Deformation microstructure of CrN and CrSiN coatings

Cross-sectional TEM micrographs of samples deformed by indentation using a spherical indenter at a load of 500 mN for all four samples are shown in Fig. 5. Different deformation microstructures can be seen in each of the samples, suggesting that deformation mechanism may vary with silicon content. Fine intercolumnar cracks, as a result of intercolumnar shear sliding, were observed in the binary CrN, CrSiN-1 and CrSiN-2 coatings (Fig. 5(a)–(c)), which all exhibit columnar grain structures. The density and locations of these intercolumnar cracks

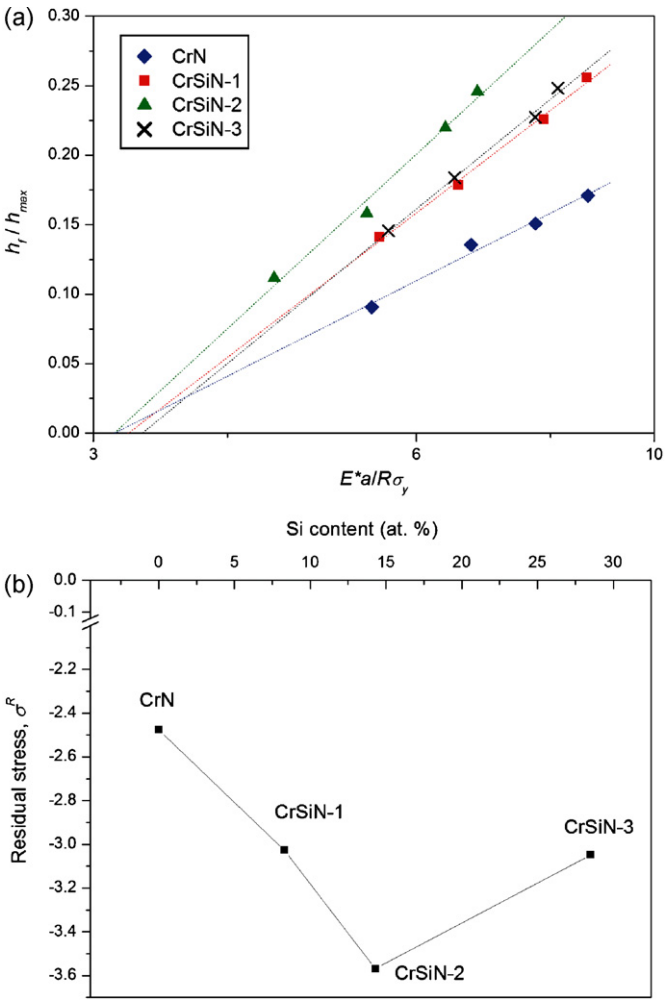

Fig. 4. (a) A plot of h_f/h_{max} versus $E^*a/R\sigma_y$ for the four samples showing the influence of residual stress in the coatings on the relative amount of elastic and plastic deformation in the samples h_f/h_{max} as a function of indentation size (a). The dotted lines are least squares regression curve fits of the experimental data (solid symbols) to the form $h_f/h_{max} = A + B \cdot \ln(E^*a/R\sigma_y)$ where A and B are curve fitting constants; (b) residual stress in the four CrSiN coatings as a function of Si content.

in these three samples are, however, slightly different. For the binary CrN coating, cracks are observed only at the edge of the indenter-sample contact and are relatively short (indicated as 'a' and 'b' in Fig. 5(a)). These cracks, shown at higher magnifications in Fig. 6, are between 130 and 240 nm long and occurred mostly along grain boundaries, but did not propagate to the bottom of this coating. A higher density of intercolumnar cracks that spread across the indented area can be observed in CrSiN-1 (Fig. 5(b)) and most of them are continuous across the thickness of the CrSiN layer (Fig. 7). Some of these through-thickness cracks even extend into the Cr wetting layer (Fig. 7(b)). In these cases, a 'step' at the Cr–substrate interface can be observed (Fig. 7(b)). Through-thickness intercolumnar cracks and shear steps were also observed in CrSiN-2 (Figs. 5(c) and 8(a)). Radial cracks, that appear to have initiated from the interface between the CrSiN coating and the Cr buffer layer, can also be identified propagating towards the middle of the indent in this sample (Fig. 8(b)). In addition, the dislocation density in the Cr buffer layer, where radial cracks occurred, appears to be much higher than that in the neighbouring undeformed area (Fig. 8(b)). In the sample with highest Si content (CrSiN-3), a large number of through-thickness cracks can be seen (Fig. 5(d)). These cracks are much wider compared to those observed in the other

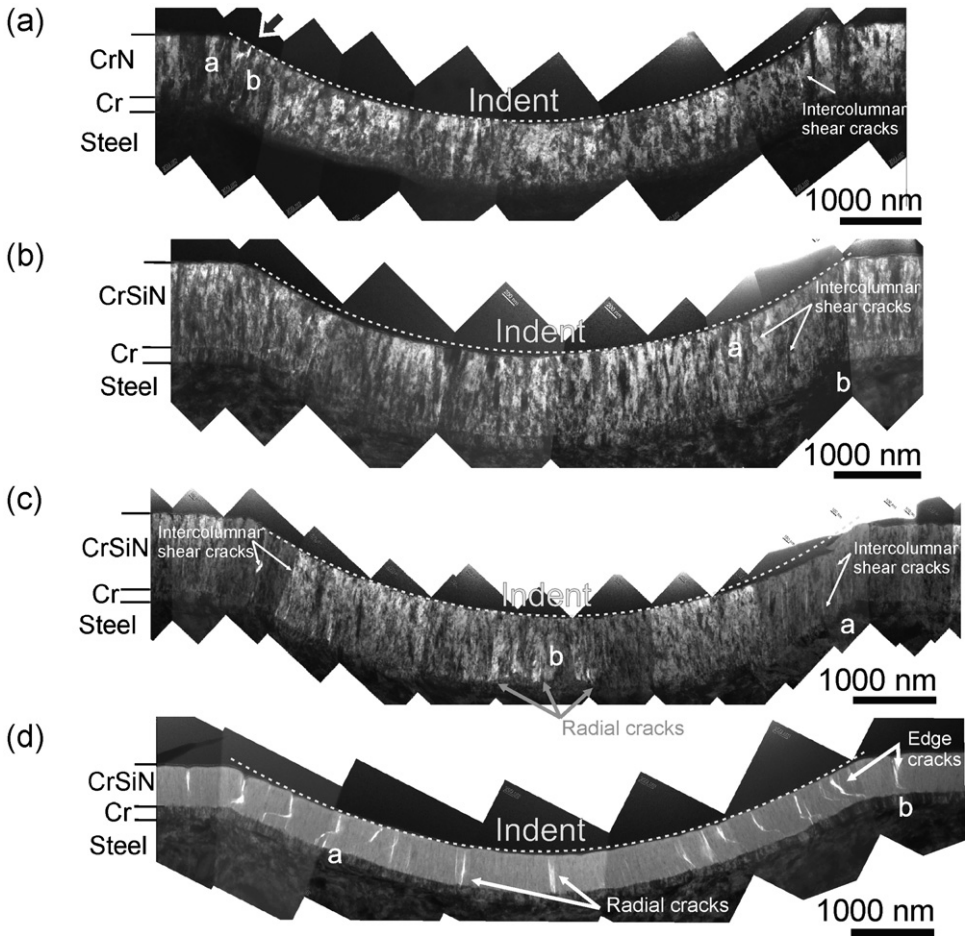

Fig. 5. Montages of TEM micrographs showing cross-sections of spherical indents made with a load of 500 mN obtained from (a) the binary CrN coating, (b) CrSiN-1, (c) CrSiN-2 and (d) CrSiN-3.

samples. The cracks, towards the middle of the indent, are parallel to the film growth direction, whereas those near the edge are step-like (Fig. 9(a) and (b)). These two types of cracks are identified to be radial and edge (or inclined) cracks, respectively, which are commonly observed in hard coatings following nanoindentation [14,31,34]. Almost all the cracks in this sample were arrested at the Cr buffer layer and shear steps were not observed in this sample (Fig. 9(b)).

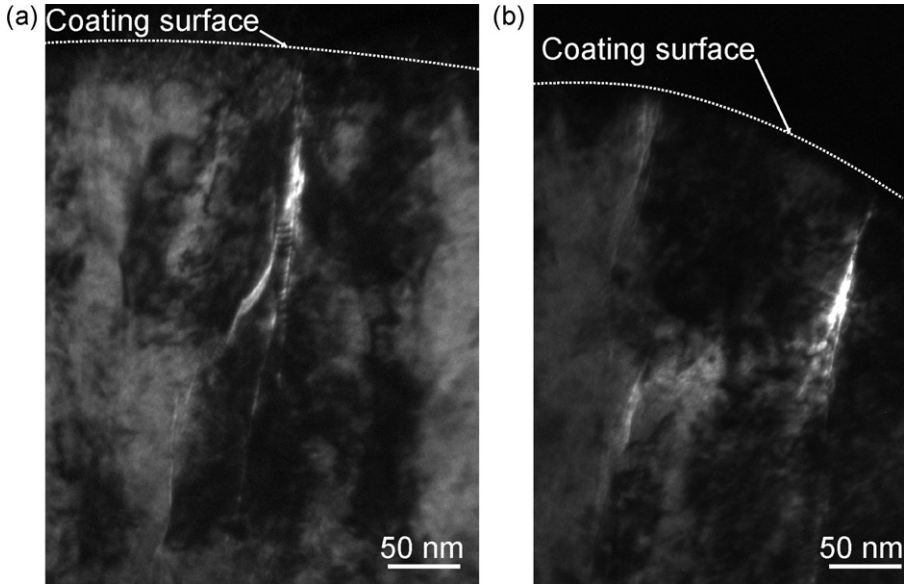

Fig. 6. Cross-sectional bright field TEM images showing intercolumnar cracks near the surface of the indented binary CrN coating. (a) and (b) correspond to the locations indicated as 'a' and 'b' in Fig. 5(a).

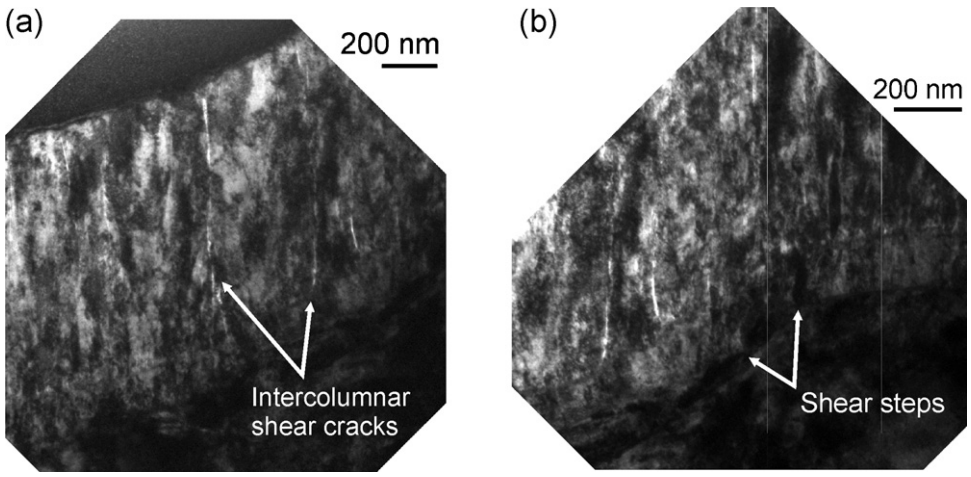

Fig. 7. Cross-sectional bright field TEM images showing through thickness intercolumnar cracks and shear step near the edge of the indenter-sample contact in CrSiN-1 after indentation. (a) and (b) correspond to the locations indicated as 'a' and 'b' in Fig. 5(b).

In addition to the formation of cracks, a significant reduction in the thickness of the films can be observed all four samples following nanoindentation (Table 5), suggesting considerable plastic deformation occurred in both the CrSiN layer and the Cr wetting layer of the coatings to accommodate the applied stress.

4. Discussion

As expected, the addition of Si to CrN exhibits an influence on the microstructure of the coatings studied here, including a significant reduction of grain size of CrN (Fig. 1), the formation of Si_3N_4 and an increase in the volume fraction of Si_3N_4 (Fig. 2 and Table 4) The overall microstructure changed from columnar grains in CrN into a structure having nanocrystals of CrN embedded in an amorphous Si_3N_4 matrix, at the highest silicon content. Although not obvious from the TEM results, a considerable volume of Si_3N_4 was detected using XPS in CrSiN-1 and CrSiN-2 (Table 4). Since crystals other than CrN were not identified from the corresponding diffraction patterns obtained from the TEM (Fig. 1(b) and (c)) the Si_3N_4 observed from XPS is likely to be amorphous in nature. It is believed that the Si_3N_4 may be segregated to the boundaries as a thin layer between the columnar CrN grains in these samples.

A similar evolutionary change in microstructure due to the increase in Si content in CrSiN coatings has been reported elsewhere [2,6,9,12]. Such microstructural changes are expected to impose influences on the residual stress and deformation mechanisms in the coatings, which may explain the dependence of mechanical behaviour (here we focused on hardness) on the coating microstructure in the samples.

4.1. Effect of Si content on residual stress in the coatings

Residual stress increased from −2.5 GPa in the binary coating to −3.6 GPa in CrSiN-2. The higher residual stress in CrSiN-1 and CrSiN-2 may be explained by the presence of Si_3N_4 (Table 4) in these two samples. The mismatch of the coefficient of thermal expansion between Si_3N_4 and CrN may generate additional thermal stresses that increase the residual stress in these coatings. In addition, a solid solution of Si in the CrN lattice was observed in these two samples, that may further increase the internal stress caused by lattice distortion [9]. It is also known that the intake of non-stoichiometric atoms in nitride films of transition metals is grain orientation dependent [23]. It was shown from the TEM diffraction patterns that CrSiN-2 exhibits smaller grains in a more random orientation compared to the sample having a lower Si content (CrSiN-1). The larger number of grains in the sample with the higher Si content would thus experience a larger degree of non-uniform lattice distortion and this would lead to higher strain within this sample. Because of this, the compressive stress in the coating reached a maximum of −3.6 GPa in CrSiN-2. Compressive stress in the coating reduced to a level similar to that measured in the CrN coating (−2.5 GPa) as the Si content (CrSiN-3) was further increased to the highest level. Despite the present of Si_3N_4 in this sample, the dramatic reduction of crystal size (Fig. 1(d)) may reduce the distortion from the thermal mismatch between Si_3N_4 and CrN and so lead to a lower residual stress. In addition, according to both TEM (Fig. 1(d)) and XPS (Table 4) analysis, this coating had a very high volume fraction of amorphous Si_3N_4, which exhibits a disordered structure with low density that could not sustain a high residual stress, resulting in the formation of the fine cracks that were observed only in this sample (Fig. 1(d)). These cracks may become visible in the XTEM images as the result of relaxation from

Table 5
Thickness of the CrSiN and Cr wetting layer in coatings measured from XTEM images at the indents (Fig. 5).

	Total thickness	CrSiN layer only	Cr layer only[a]	Percentage thickness reduction (compare to measurements in Table 2)	
				Total	Fraction from CrSiN layer
Binary CrN (0 at.% Si)	0.863 ± 0.069	0.755 ± 0.054	0.108	14.0%	70.2%
CrSiN-1 (8.3 at.% Si)	1.082 ± 0.037	0.925 ± 0.030	0.157	7.5%	67.0%
CrSiN-2 (14.5 at.%Si)	0.998 ± 0.038	0.867 ± 0.038	0.131	6.5%	72.5%
CrSiN-3 (28.3 at.% Si)	0.615 ± 0.020	0.478 ± 0.011	0.137	4.1%	65.3%

[a] Thickness of the Cr layer is calculated from total thickness – thickness of CrSiN layer.

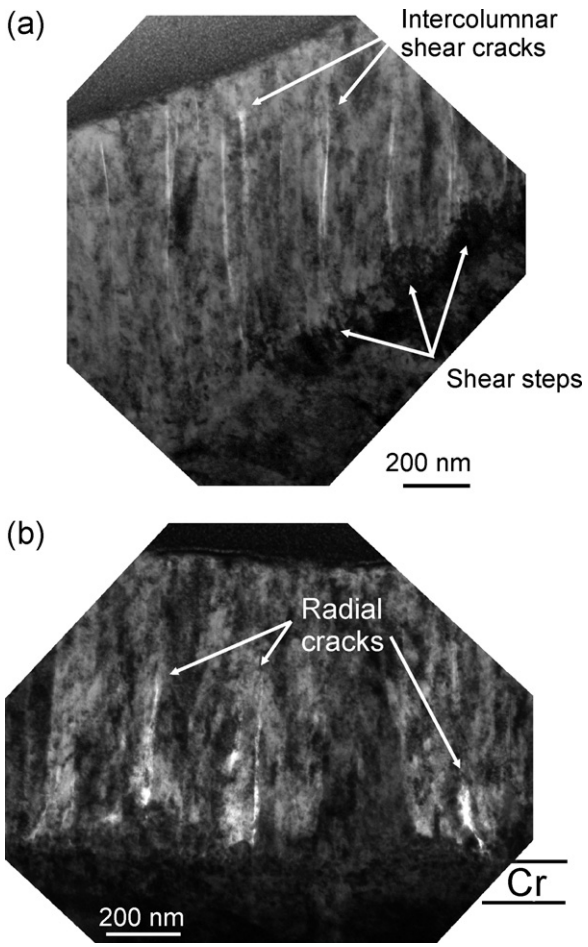

Fig. 8. Cross-sectional bright field TEM images showing (a) through thickness intercolumnar cracks and shear step near the edge of the indenter-sample contact and (b) radial cracks and high density of dislocations near the centre of the indent in the deformed coating of CrSiN-2. (a) and (b) correspond to the locations indicated as 'a' and 'b' in Fig. 5(c).

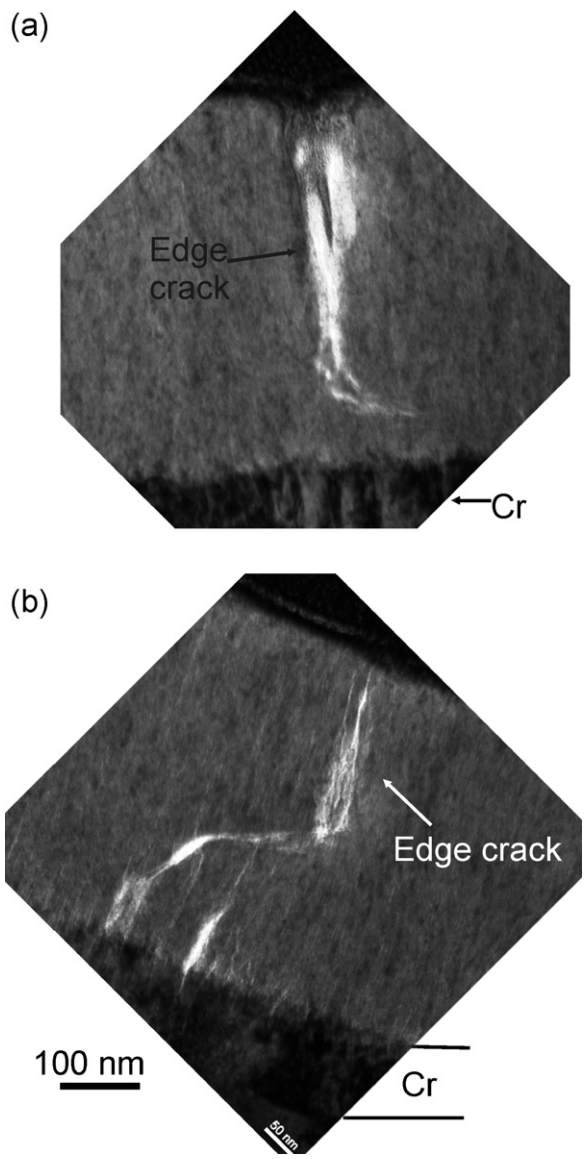

Fig. 9. Cross-sectional bright field TEM images of edge cracks observed in the indentedCrSiN-3 coating. (a) and (b) correspond to the locations indicated as 'a' and 'b' in Fig. 5(d).

the residual stresses in the coating during the XTEM sample preparation [35]. Although a similar, or higher, level of compressive stress was also observed in the coatings with lower Si contents, most of the internal stress may be accommodated by formation of crystal defects, e.g. dislocations in CrN grains in samples with lower Si contents. In CrSiN-3, the CrN crystals are too small to accommodate the high stress by formation of defects and this leads to the generation of cracks in the brittle Si_3N_4 matrix instead.

4.2. Deformation mechanisms of the coatings

Three major deformation mechanisms following indentation were observed in the four coatings: plastic deformation, intercolumnar shearing and crack formation. Plastic deformation observed in all four samples is expressed by reduction in coating thickness (Table 5). Considerable thickness reduction (14% reduction in total thickness, in which a fraction of 70.2% was due to the thickness reduction of the CrN layer) was observed in the binary CrN coating and the percentage of thickness reduction in the CrSiN coatings reduced as the Si content in the coating increased. The reduction in degree of plastic deformation in the coating having high Si contents is possibly due to the increase in the volume of the stiffer Si_3N_4 phase.

Intercolumnar shear occurred in the binary CrN, CrSiN-1 and CrSiN-2 coatings to differing extents, since intercolumnar cracks and shear steps at coating–substrate interface can be observed in these three samples. Through thickness cracks were observed in the deformed CrSiN-1 coating, but most of the intercolumnar cracks in the binary sample were arrested in the middle of the film (Fig. 6). This may be related to the high compressive residual stress (Fig. 4(b)) [35] and large amount of plastic deformation (Table 5) in this coating. Despite the slightly higher residual stress, through-thickness cracks were observed in CrSiN-1. This may be because although the grains in this sample remain columnar, they tend to align in a parallel manner, which provide an easy pathway for the propagation of intercolumnar cracks.

Intercolumnar shear was also observed in CrSiN-2, but no significant shear steps can be seen. This is probably because of the increase in volume of Si_3N_4 (Table 4) between the CrN grains that restrain the shear between grain boundaries. At the same time, the formation of radial and edge cracks are observed, possibly due to the brittleness arising from the higher volume of Si_3N_4.

In the sample having the highest Si content (CrSiN-3), the volume of the Si_3N_4 phase was similar to that of the CrN phase. The CrN crystals were ~20 nm in diameter, which may not be deformed easily by formation and movement of dislocations. Therefore, most

deformation occurred in the amorphous Si_3N_4 matrix that showed a brittle type of deformation, including edge and radial cracks.

4.3. Hardening due to Si addition in CrN

It is known that the hardness of a material depends on the deformation mechanisms that are in operation. In addition, hardness measured by nanoindentation is also known to be influenced by residual stress in the testing materials. Materials exhibit compressive residual stress showed higher hardness according to the principle of plasticity [16]. Provided that the samples have similar microstructures and thickness, those having higher compressive residual stress are expected to show higher hardness. In this study, the binary CrN and CrSiN-1 coatings deformed primarily by intercolumnar shearing. Although the propagation of intercolumnar cracks in CrSiN-1 appears easier than in the binary CrN sample, these two samples showed similar hardness values (Fig. 3(a)). This may be because of the slightly higher compressive residual stress in CrSiN-1.

In this study, CrSiN-2 exhibits the highest hardness. Since intercolumnar shear was observed in the indented sample (Figs. 5(c) and 8(a)), the high hardness is possibly due to the combined effect of grain boundary strengthening by Si_3N_4 segregation, hardening due to Si as a solid solution strengthener in CrN and the finer grain size compared to the binary CrN coating and CrSiN-1. In addition, both the solid solution of Si and the fine grain structure in this sample may also contribute to a relatively high compressive residual stress that inhibits intercolumnar shear and so leads to a higher hardness.

The sample having the highest Si content (CrSiN-3) does not exhibit columnar grains and so the hardness is primarily governed by the Hall–Petch relationship. The hardness is reduced as the Si content in the coating was increased to 28.5 at.%, despite the apparently smaller grain size in this sample (Fig. 1(d)). This is likely to be due to the high volume fraction of Si_3N_4 in this sample (Table 4). In addition to the intrinsic brittleness of Si_3N_4, due to its relatively open structure, the high density of fine through-thickness cracks in the as-deposited coating may also contribute to the lower hardness when the indentation is made near some of these pre-existing cracks even at low indentation depth (<10% of film thickness). The low value of elastic modulus of this coating (Fig. 3(b)) is also likely to be related to the presence of these pre-existing cracks.

4.4. Oxide layer on the surface

A high oxygen content (>30 at.%) was observed from the near surface region of the as-deposited coatings (Table 3). Since XPS can only detect signal from the outer ~10 nm from the surface region, the thin layer observed from XTEM in all samples is likely a native oxide, similar to that observed in other CrN coatings [26,27]. Analysis of the XPS spectrum near the O 1s peak confirmed that this layer is mainly composed of Cr—O—N and Cr_2O_3, consistent with other studies [36,37,26]. Some —OH bonding, likely to be due to the adsorption and decomposition of water from the ambient environment (air) [37,26], was also detected in all the coatings with, and without, Si additions. For samples having Si contents, some O was bonded to Si to form SiO_x. Molecular N, which had been also observed in some CrN coatings in the literature [36,38] was not observed in the samples here, suggesting that the oxide layer in the current coatings is likely to be stable and formed very soon after deposition [26].

4.5. Strengthening by addition of Si in CrN compare to TiSiN

Comparing the hardness of the four samples used in this study, there was only a small increase in hardness by ~6 GPa due to the addition of Si. Although a nanocomposite microstructure was successfully attained by the addition of Si content to a higher level, the hardness of the coating with the highest Si content (CrSiN-3) was lower than that of the coating having 14.3 at.% Si in CrSiN-2 (Fig. 3(a)).

In the literature, there have been a number of suggestions to explain the lower hardness in CrSiN compared to TiSiN [3,7,8]. Firstly, binary CrN is not as hard as TiN [8]. Observations in this study showed significant thickness reduction in both the CrSiN layer and the Cr wetting layer following indentation of all four coatings (Table 5), suggesting that plastic deformation occurred in both CrN columnar grains and Cr grains in the wetting layer. By comparison such plastic deformation is usually not observed in TiSiN coatings [15,39]. It has also been suggested that the covalent bonding between nanocrystals of CrN and the amorphous Si_3N_4 phase is much weaker than that between TiN and Si_3N_4 [3]. As discussed above, the Si_3N_4 phase detected in CrSiN-1 and CrSiN-2 in this study is likely to be located between CrN grains. Thus, a weaker boundary between Si_3N_4 and CrN would lead to easier intercolumnar shearing and so lower hardness.

Further, extreme purity of the coating is required to achieve superhardness in TiSiN [40,41]. It was found that a traces of oxygen of only 0.1 at.% may lead to a dramatic drop of hardness from ~80 GPa to ~30 GPa [40]. In the samples studied here, oxidation occurred at least on the surface layer. Since indentation for hardness measurement is mostly concentrated at the surface, the oxide layer apparently reduce the measured hardness. Also, it is very likely that the oxygen content in the near surface region may be significant and so may lower the hardness.

5. Conclusion

The microstructure, residual stress and hardness of CrSiN coatings with differing Si contents deposited in a closed field unbalanced magnetron sputtering system were studied. It was found that as the Si content increased, the grain size of the CrN reduced and a nanocomposite structure consisting of nanocrystals of CrN embedded in an amorphous matrix was achieved when the Si content was 28.5 at.%. TEM examination of the microstructure of the indented samples showed that samples that exhibited columnar grain structures primarily deformed by intercolumnar shear. Whereas the sample showing the nanocomposite-like structure deformed by formation of radial and edge cracks due to the high volume fraction of amorphous phase, assisted by the dense fine cracks that probably due to high residual stress in this film. In this study, the highest hardness was achieved when the Si content in the film was ~14.3 at.%, which is likely to be a combined hardening effect due to grain boundary strengthening by Si_3N_4 segregation, small grain size, solid solution of Si in CrN and high residual stress in this sample.

Acknowledgement

The authors would like to thank the Australian Microscopy and Microanalysis Research Facilities (AMMRF) for financial support on this study.

References

[1] L. Cunha, M. Andritschky, K. Pischow, Z. Wang, Thin Solid Films 355–356 (1999) 465–471.
[2] G.S. Kim, S.M. Kim, S.Y. Lee, J. Vac. Sci. Technol. A A27 (2009) 873–879.
[3] E. Martinez, R. Sanjines, A. Karimi, J. Esteve, F. Levy, Surf. Coat. Technol. 180–181 (2004) 570–574.
[4] J. Patscheider, T. Zehnder, M. Diserens, Surf. Coat. Technol. 146–147 (2001) 201–208.
[5] S. Veprek, Surf. Coat. Technol. 97 (1997) 15–22.

[6] H.Y. Lee, W.S. Jung, J.G. Han, S.M. Seo, J.H. Kim, Y.H. Bae, Surf. Coat. Technol. 200 (2005) 1026–1030.
[7] J.-W. Lee, Y.-C. Chang, Surf. Coat. Technol. 202 (2007) 831–836.
[8] M. Benkahoul, P. Robin, S.C. Gujrathi, L. Martinu, J.E. Klemberg-Sapieha, Surf. Coat. Technol. 202 (2008) 3975–3980.
[9] D. Mercs, P. Briois, V. Demange, S. Lamy, C. Coddet, Surf. Coat. Technol. 201 (2007) 6970–6976.
[10] E. Martinez, R. Sanjines, O. Banakh, F. Levy, Thin Solid Films 447–448 (2004) 332–336.
[11] Y.H. Yoo, J.H. Hong, J.G. Kim, H.Y. Lee, J.G. Han, Surf. Coat. Technol. 201 (2007) 9518–9523.
[12] Q.M. Wang, K.H. Kim, Acta Mater. 57 (2009) 4974–4987.
[13] D. Gall, C.-S. Shin, T. Spila, M. Odén, M.J.H. Senna, J.E. Greene, I. Petrov, J. Appl. Phys. 91 (2002) 3589–3597.
[14] Z.H. Xie, M. Hoffman, P. Munroe, A. Bendavid, P.J. Martin, Acta Mater. 56 (2008) 852–861.
[15] P.C. Wo, P.R. Munroe, Z.F. Zhou, K.Y. Li, Z.H. Xie, Mater. Sci. Eng. A 527 (2010) 4447–4457.
[16] J.G. Swadener, B. Taljat, G.M. Pharr, J. Mater. Res. 16 (2001) 2091–2102.
[17] T. Matsue, T. Hanabusa, Y. Ikeuchi, Thin Solid Films 281–282 (1996) 344–347.
[18] M.S. Ahmed, X. Zhao, Z.-F. Zhou, P. Munroe, N. Chen-Tan, L. Kwok, Y. Li, Z. Xie, J. Am. Ceram. Soc. 94 (2011) 1546–1551.
[19] M. Gelfi, G.M. La Vecchia, N. Lecis, S. Troglio, Surf. Coat. Technol. 192 (2005) 263–268.
[20] P.H. Mayrhofer, G. Tischler, C. Mitterer, Surf. Coat. Technol. 142–144 (2001) 78–84.
[21] D.A. Shirley, Phys. Rev. B: Solid State 5 (1972) 4709–4714.
[22] W.C. Oliver, G.M. Pharr, J. Mater. Res. 7 (1992) 1564–1582.
[23] I. Goldfarb, J. Pelleg, L. Zevin, N. Croitoru, Thin Solid Films 200 (1991) 117–127.
[24] J.C. Oliveira, A. Manaia, J.P. Dias, A. Cavaleiro, D. Teer, S. Taylor, Surf. Coat. Technol. 200 (2006) 6583–6587.
[25] D. Güttler, B. Abendroth, R. Grötzschel, W. Möller, Appl. Phys. Lett. 85 (2004) 6134–6136.
[26] L. Cunha, M. Andritschky, L. Rebouta, K. Pischow, Surf. Coat. Technol. 116–119 (1999) 1152–1160.
[27] M. Grundner, J. Halbritter, J. Appl. Phys. 51 (1980) 397–405.
[28] A. Lippitz, T. Hubert, Surf. Coat. Technol. 200 (2005) 250–253.
[29] J.F. Moulder, W.F. Stickle, P.E. Sobol, K.D. Bomben, Hand-book of X-ray Photoelectron Spectroscopy, 1992.
[30] K. Yamamoto, Y. Koga, S. Fujiwara, Diamond Relat. Mater. 10 (2001) 1921–1926.
[31] S. Bhowmick, Z.H. Xie, M. Hoffman, V. Jayaram, S.K. Biswas, J. Mater. Res. 19 (2004) 2616–2624.
[32] B. Taljat, G.M. Pharr, in: R. Vinci, O. Kraft, N. Moody, E. Shaffer II (Eds.) Mater. Res. Soc. Symp. Proc. (2000) 519.
[33] K.L. Johnson, Contact Mechanics, Cambridge University Press, Cambridge, 1987.
[34] S. Bhowmick, A.N. Kale, V. Jayaram, S.K. Biswas, Thin Solid Films 436 (2003) 250–258.
[35] L.W. Ma, J.M. Cairney, M. Hoffman, P.R. Munroe, Surf. Coat. Technol. 192 (2005) 11–18.
[36] E. Huber, S. Hofmann, Vacuum 45 (1994) 1003–1005.
[37] A. Conde, A.B. Cristóbal, G. Fuentes, T. Tate, J. de Damborenea, Surf. Coat. Technol. 201 (2006) 3588–3595.
[38] F. Esaka, K. Furuya, H. Shimada, M. Imamura, N. Matsubayashi, H. Sato, A. Nishijima, A. Kawana, H. Ichimura, T. Kikuchi, J. Vac. Sci. Technol. A 15 (1997) 2521–2528.
[39] Z.H. Xie, M. Hoffman, P. Munroe, R. Singh, A. Bendavid, P.J. Martin, J. Mater. Res. 22 (2007) 2312–2318.
[40] S. Veprek, H.-D. Mannling, A. Niederhofer, D. Ma, S. Mukherjee, J. Vac. Sci. Technol. B 22 (2004) L5–L9.
[41] S. Veprek, M.G.J. Veprek-Heijman, P. Karvankova, J. Prochazka, Thin Solid Films 476 (2005) 1–29.